Metals and Materials International (2024) 30:2972–2981
https://doi.org/10.1007/s12540-024-01707-8

On the Damping Performance and Mechanical Response of Additive-Manufactured and Thermo-Mechanical Processed AlSiMg Alloy

Canay Isil[1,2] · Amin Radi[1,2] · Guney Guven Yapici[1,2,3]

Received: 31 December 2023 / Accepted: 22 April 2024 / Published online: 30 May 2024
© The Author(s) 2024

Abstract
Recent advancements in additive manufacturing (AM) fuel efforts for expanding the design envelopes for components obtained via this technology through continuous improvement in mechanical behavior. Damping properties can also be altered depending on the microstructure evolved during AM. Therefore, achieving enhanced monotonic mechanical response with better damping properties is highly sought-after. In this respect, thermo-mechanical processing via severe plastic deformation (SPD) and artificial aging is imparted on the additive-manufactured samples with the target of grain refinement and densification to further improve mechanical and damping properties. Employing microstructural characterizations and mechanical experiments, a multi-scale exploration is carried out to develop a relation between the evolved microstructure and the resulting behavior. It is concluded that introducing a refined microstructure decorated with well-distributed (Mg,Si)-rich phase and favorable dislocation substructure in AlSi10Mg positively affects the resulting mechanical behavior. Moreover, it is shown that artificial aging can be employed to improve the damping characteristics of severely deformed additive-manufactured AlSi10Mg alloy.

Keywords Additive manufacturing (AM) · AlSi10Mg · Damping properties · Severe plastic deformation (SPD) · Nano-indentation · Thermo-mechanical processing

1 Introduction

Aluminum alloys have been investigated vastly for their unique mechanical characteristics and their suitability to be additive-manufactured for gaining design freedom and the ability for precise and rapid fabrication [1, 2]. As a typical manufacturing route, selective laser melting (SLM) which is a laser powder bed fusion (LPBF) process inherits a significant drawback. The SLM method potentially introduces a systematic void structure in components fabricated with AlSi10Mg and AlSi alloys [3–5]. Recognizing the inevitability of the porosity in SLMed alloys, it becomes essential to identify the effect of the impacts of porous and dense structures on mechanical characteristics. A thorough investigation into the influence of porosity on the mechanical characteristics of alloys produced by LPBF methods indicates the possibility of tensile strength enhancement via porosity reduction. However, it has also been established that beyond a certain threshold, the predominant factor influencing tensile strength shifts to the microstructural characteristics of the alloy [6]. Thermo-mechanical processing (TMP) is a viable technique for microstructural engineering and can be utilized to define the routes for achieving advanced mechanical response in additive-manufactured alloys. In essence, TMP can provide insight to design alloys for additive manufacturing and assist with revealing the vast potential of additive-manufactured alloys [7, 8].

Within this context, the utilization of severe plastic deformation (SPD) methods could lead to remarkable outcomes for property improvement. These improvements can be

Canay Isil and Amin Radi have contributed equally.

✉ Guney Guven Yapici
guven.yapici@ozyegin.edu.tr

[1] Mechanical Engineering Department, Ozyegin University, Istanbul, Türkiye

[2] Mechanics and Manufacturing of Functional and Structural Materials Laboratory (MEMFIS), Ozyegin University, Istanbul, Türkiye

[3] Center for Additive Manufacturing Alloys (KIMTAL), Ozyegin University, Istanbul, Türkiye

primarily attributed to the introduction of a high dislocation density substructure along with a favorable grain size distribution in the micro and nano regime [9–11]. Moreover, it has recently been reported that equal channel angular extrusion/pressing (ECAE/P) can be employed as a viable processing tool for eliminating the remnant voids after LPBF [12, 13]. In the case of AlSi10Mg alloys additive-manufactured through SLM, the application of proper heat treatments presents a promising path for achieving a well-balanced improvement in mechanical properties [14]. It has also been disclosed that by the re-arrangement of the silicon-network in AlSi eutectic alloys, noticeable enhancement in mechanical behavior can be obtained via suitable thermo-mechanical processing [15–18]. Since heat treatments can effectively alter the phase formation kinetics and the accompanying distribution of elements present in the microstructure and limit the dislocation movement [19, 20]; heat input during SPD processing shall have a profound impact on the final mechanical behavior as dictated by the grain size distribution, the formation of (Mg,Si)-rich phase, and the evolution of the silicon network in the microstructure.

Besides the enhanced mechanical properties of the additive-manufactured alloys, some systematic studies in lattice structures exploring the damping, vibration, and acoustic properties have reported promising results [21, 22]. The damping capacity of the material is the ability to absorb mechanical vibrations and dissipate them in the form of thermal energy [23, 24]. By taking advantage of the lightweight structure of AM parts, the damping behavior of the components is one of the essential design factors for various industrial applications. Rosa et al. [25] have reported that SLM 316L specimens with lattice structures have shown superior damping capability compared to the bulk specimens depending on the amplitude-dependent internal friction behavior. It is clear that AM technologies provide additional functionalities according to the design targets and the materials used therein. Wang et al. have presented that the layer-structured NiTi shape memory alloy manufactured via SLM has better damping properties than the rolled alloy [26].

Aluminum alloys have a wide range of application areas with advantageous properties such as high specific strength, machinability, and lightweight structure. In order to complement these properties with high damping capacity in an aluminum alloy, numerous research has been reported [27]. For that matter, AM of aluminum alloys is similarly investigated due to the aforementioned interest in this rapidly developing technology [28, 29]. One of the biggest challenges of the AM methods is the rapid cooling, thus solidification leading to higher residual stress levels in the microstructure [30]. For that matter, it is reported that the application of post-processing can enhance the mechanical behavior of additive-manufactured AlSi10Mg and almost reach a level of conventional-manufactured alloy [31]. In another work, the internal friction (Q^{-1}) and dynamic modulus levels of the as-cast and the as-built AlSi10Mg alloys are compared to find out that the latter demonstrates a better damping response [32]. Recently, a comprehensive study has presented that employing thermal treatments to SLM AlSi10Mg samples can provide an advantage in adjusting the damping capacity [33].

As a first-time attempt, this study discloses a structure–property relation between the mechanical behavior and the damping characteristics of the additive-manufactured AlSi10Mg alloy subjected to different thermo-mechanical treatments. In order to address the damping behavior, relevant experiments were performed under a wide range of temperatures and different strain amplitudes, while the mechanical response is tracked at various scales. Property wise, strength and damping capacity originate from opposing mechanisms; while the restriction of dislocation movement promotes strength, damping capacity is supported by the movement of dislocations. Consequently, these two properties are often mutually exclusive. Therefore, as a novel contribution, this work defines the microstructural features to be attained in additive-manufactured AlSi10Mg for improving the mechanical properties while attaining decent damping properties.

2 Experimental Procedure

A commercially available LPBF system was employed to fabricate the AlSi10Mg alloy samples with the SLM parameters as follows: scanning speed of 1300 mm/s, power of 370 W, layer thickness of 30 µm, and hatch spacing of 190 µm. Additive-manufactured AlSi10Mg blocks with dimensions of $20 \times 20 \times 100$ mm were severely deformed via ECAP at 200 °C for four passes following Bc route [11]. The ECAP die is equipped with a 90-degree channel imparting severe shear strain up to 1.16 per pass. Billets were inserted in the die with the longitudinal direction (LD) parallel to the SLM building direction (BD). During each step, the billets were kept for 15 min inside the ECAP die, and they were quenched in water after each pass. The die temperature was constant during ECAP processing and monitored by thermocouples. Samples were cut via electro-discharge machining (EDM) from the as-built and the ECAP billets, then were ground using SiC papers up to 4000. A group of samples were aged at 180 °C for 2 h and are named as ECAP-Aged. The density measurement of the samples was done according to the Archimedes method. The reference and second fluid were selected as air and distilled water, respectively. The samples were cleaned in an ultrasonic bath prior to the measurements. The density of the samples was calculated by Eq. 1 given below:

$$\rho_s = \frac{m_{air}}{m_{air} - m_{fluid}} x\left(\rho_{fluid} - \rho_{air}\right) + \rho_{air} \quad (1)$$

where ρ_{fluid} is 0.9982 g/cm^3, ρ_{air} is 0.0012 g/cm^3 (at 20 ± 2 °C), m_{air} is the mass of the samples in air and m_{fluid} is the mass of the samples in water. The measurements are repeated five times with three different samples for each condition. The dog-bone-shaped samples for mechanical tests were prepared with dimensions of 15 mm gage length, 3 mm gage width, 2 mm thickness, and 30 mm total length. Uniaxial tensile tests were performed utilizing an Instron servo-hydraulic mechanical testing frame at room temperature with a strain rate of 10^{-3} s^{-1}. An extensometer with a measuring length of 10 mm was employed during the monotonic tests. Three samples were tested for each condition during tensile tests. Vickers hardness tests were applied with a load of 100 gf for 15 s.

The damping properties were examined with a PerkinElmer dynamic mechanical analyzer (DMA) within a temperature range from 0 to 300 °C with a heating rate of 5 °C/min. To determine the internal friction, Q^{-1}, rectangular prism samples size 36 mm × 8 mm × 1 mm were used employing a single cantilever mode with a constant frequency of 1 Hz, where the strain amplitude γ was selected as 5×10^{-5}, and the tests were performed during the heating step. The strain amplitude γ test was carried out with varying amplitudes from 1×10^{-4} to 5×10^{-4}. The microstructural analysis was performed employing a Zeiss Gemini high-resolution scanning electron microscope (SEM) equipped with electron backscatter diffraction (EBSD) on as-built and ECAP conditions. EBSD analysis was performed at 20 kV and the samples were studied at step sizes of 1250 nm and 100 nm for as-built and ECAP conditions, respectively, after applying oxide polishing suspension with a grit size of 0.04 µm for 16 h.

The indentation response of the samples was measured using an Anton Paar nano-indentation tester employing a diamond Berkovich tip with an elastic modulus of 1140 GPa. Prior to tests, samples were mechanically grounded using SiC papers and were polished with 0.02 µm colloidal silica for 3 h. The calibration of the instrument was performed using a standard fused silica sample. The study involved a 10 × 10 matrix of indents with a spacing of 50 µm in both x and y directions. The indentation load for all samples was 40 mN, and loading and pause time was selected as 10 s and 5 s, respectively.

3 Results and Discussion

3.1 Microstructural Evolution

The results from the Archimedes density measurements are reported in Table 1. It can be observed that SPD via ECAP increases the density of the additive-manufactured samples. Moreover, the density of the ECAP-Aged sample showed a slight increase owing to the aging treatment which supports densification due to the heat input thereby leading to the highest density level [14, 34]. All measurements are found to be in good agreement with the theoretical density value.

The XRD results of the samples are shown in Fig. 1a**.** As represented in the results, all samples contain aluminum (Al) phase besides silicon (Si). It is clear that the microstructures, through severe plastic deformation and artificial aging, do not indicate the existence of new phases in the alloy system. However, it can be disclosed that depending on the thermo-mechanical processing, the intensity levels of Mg_2Si peaks can be altered. Obviously, with the advancing in fabrication processes, more (Mg,Si)-rich phase and possible Mg_2Si particles were introduced in the microstructure since the intensity of the peaks related to this phase heightened [35, 36].

EBSD studies were conducted to represent a universal examination before and after ECAP processes. Inverse pole figure (IPF) maps represent an average grain size of 10 ± 3.9 µm in the as-built microstructure (see Fig. 1b). The IPF map shows variation in grain size and morphology distribution, which is initiated by the different solidification rates during the SLM process [37]. The crystallographic texture in the as-built microstructure is introduced during directional solidification within the melt pool [38, 39]. The < 001 > direction is more likely at the center of the melt pool, and the texture is altered towards < 101 > direction adjacent to the center. However, crystals are mainly aligned along < 101 > and < 111 > directions at overlapping sections. The SLM process at each step introduced a distance of 250 µm between the pools in the microstructure. The SLM fabrication leads to distinct grain morphologies in the microstructure. The columnar grains form more likely at the middle regions during each scanning pulse (see Fig. 1b black square). On the other hand, equiaxed grains are present at overlapping regions, which are caused by re-melt-solidification cycles [40].

The acquired EBSD results for the ECAP and ECAP-Aged samples are represented in Fig. 2. The inverse pole figure (IPF) maps show a grain size of 291 ± 130 nm and 350 ± 121 nm

Table 1 The results of the Archimedes density measurements

Sample	SLM-as-built	ECAP	ECAP-aged
Density (g/cm^3)	2.56 ± 0.04	2.65 ± 0.02	2.66 ± 0.01

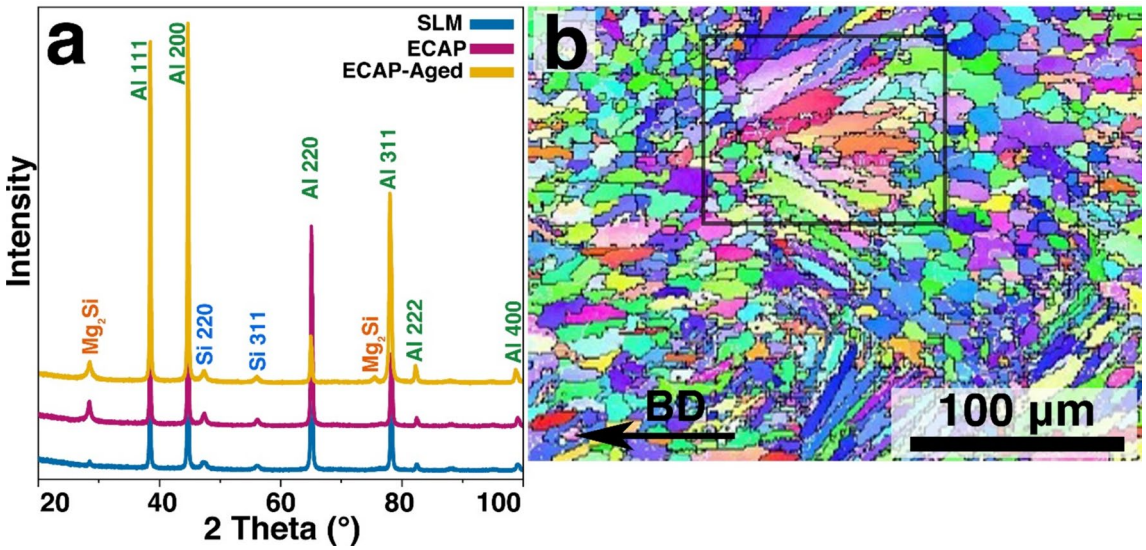

Fig. 1 **a** XRD results for the ECAP and the ECAP-Aged samples and **b** Inverse pole figure (IPF) map for the as-built sample, where BD indicates the build direction

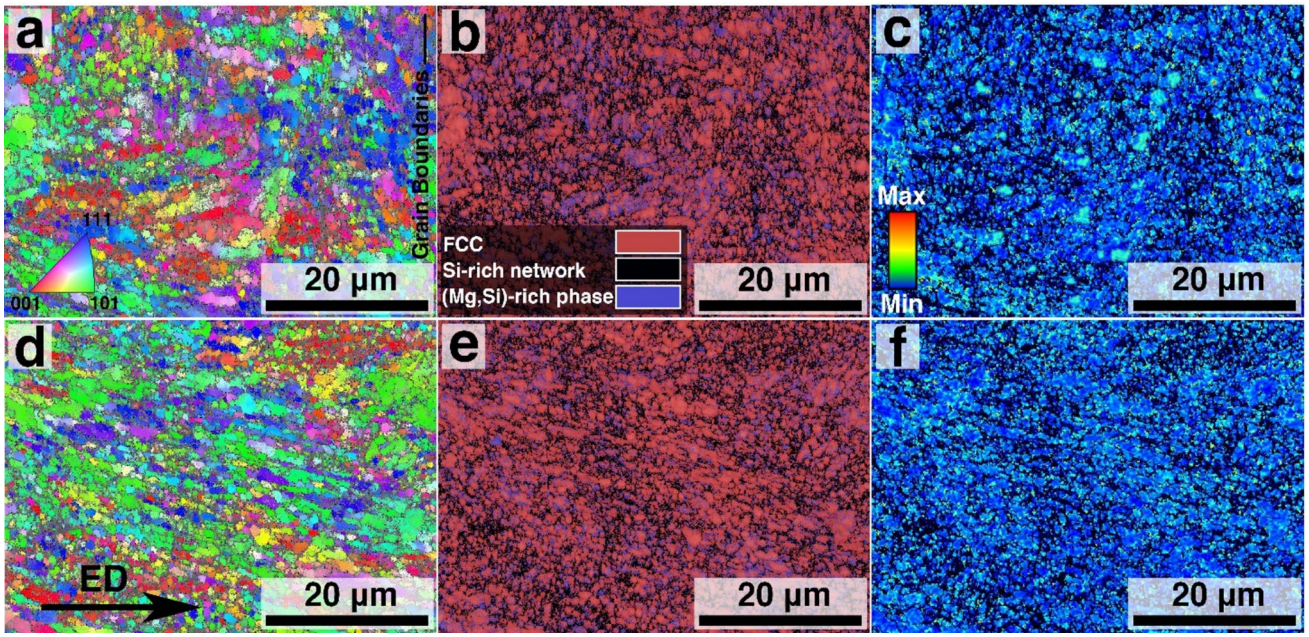

Fig. 2 Results for the ECAP sample **a** Inverse pole figure (IPF) map, **b** Phase map, and **c** Kernel average misorientation (KAM) map (values between 0 and 5), results for the ECAP-Aged **d** Inverse pole figure (IPF) map, **e** Phase map, and **f** Kernel average misorientation (KAM) map. ED indicates the extrusion direction

for the ECAP and ECAP-aged specimens, respectively (see Fig. 2a and d). It has been demonstrated that the high dislocation density generated under applied severe shear stress during ECAP and enhanced capability of cross-slip assisted dislocation movement due to high stacking fault energy (SFE) present in aluminum alloys are the two main reasons for the development of ultra-fine grain (UFG) microstructure in the examined alloy [41–43]. SPD introduces a nano-size grain distribution in the as-built microstructure and causes a Si-network having a sub-micron structure. Under the applied severe plastic deformation, there is no sign of Si-rich network agglomeration in the UFG microstructure. In contrast, the secondary phase shows different distribution with thermal treatment. Namely, a relatively more uniform distribution of the (Mg,Si)-rich phase

can be obtained in the ECAP sample after aging. The kernel average misorientation (KAM) values for the latter dropped to 0.309. This indicates that artificial aging decreases the dislocation density in the ECAP microstructure (KAM value of 0.389) and introduces a relatively more recovered structure.

3.2 Mechanical Behavior

Figure 3 shows the mechanical behavior of the conditions under monotonic tensile tests. The results show that the as-built AlSi10Mg possesses a yield strength (YS) and an ultimate tensile strength (UTS) of 165 MPa and 406 MPa, respectively. The as-built sample has an 8.4% ductility at the failing point. Results illustrate that SPD via ECAP, and proper heat treatment can improve the mechanical behavior of the additive-manufactured AlSi10Mg alloy. After processing via ECAP, YS and UTS levels are intensified to 323 MPa and 372 MPa, respectively. In other words, ECAP induced SPD was instrumental for the 95% increase of the initial YS value. Moreover, the ductility increases by 54% for the newly introduced microstructure employing ECAP. The results illustrate that there is a notable modification in the mechanical response achieved by SLM followed by ECAP process as compared to the conventional as-casted state [44]. However, artificial aging of the ECAP microstructure modified the YS and UTS values to 351 MPa and 443 MPa, respectively. This behavior can be originated from the introduction of additional secondary phase acting as obstacles limiting dislocation movement during plastic deformation and thereby intensifying the strength of the alloy. As illustrated in the ECAP-Aged condition, impediment of dislocations can act as stress concentration zones which can lead to early onset of failure.

Previous research on additive-manufactured AlSi12 demonstrated that imposing severe plastic deformation can eliminate SLM-originated porosity. Besides, the inhomogeneous microstructure introduced during AM can be improved, whereby relatively more homogeneous grain size and uniform Si-network distribution can be obtained. This in turn led to higher YS, UTS, and failure elongation levels [12]. In parallel, SPD induced strain has a similar effect on the processing-structure–property relations of AlSi10Mg under investigation. The calculated strain hardening rate (SHR) curves show that the as-built sample possesses a higher hardening rate. Besides, ECAP and ECAP-Aged samples show almost the same SHR behavior with slightly different values (Fig. 3b). The possible explanation for the higher hardening of the as-built sample is twofold. First, the high dislocation density induced during SPD is a limiting factor for the high strain hardening during post-SPD straining. Second, the Si-network present after AM can effectively interact with the dislocations introduced during tensile straining, and thus improves the strain hardening [43].

3.3 Nano-indentation Response

Figure 4 represents the nano-indentation results for all three conditions. The force-depth curves of the samples show higher hardness values for the ECAP and ECAP-Aged microstructures. Typically, mechanical characteristics exhibited at the nano-scale present a correlation with those observed at the macro-scale [45]. The results show that, unlike the two other processed conditions, the SLM-As-built sample shows an abrupt change during indentation. The illustrated "pop-in" behavior can be initiated from the micro- and nano-voids present in the as-built microstructure [12]. The pop-in behavior is observed in all indentations during map preparation. This behavior mainly occurs around the indentation depth of around 650 nm and the applied force of about 15 mN (see Fig. 4a). The acquired hardness vs. indentation depth results represent that the ECAP-Aged microstructure possesses the highest hardness. It can be disclosed that thermo-mechanical processing (ECAP-Aged) improved the hardness by up to 37%. In addition, the SLM-As-built sample, unlike the ECAP and ECAP-Aged, shows one step transition instead of multiple transitions in the hardness vs. indentation depth graph. These results represent that the apparent step in the ECAP and ECAP-Aged samples

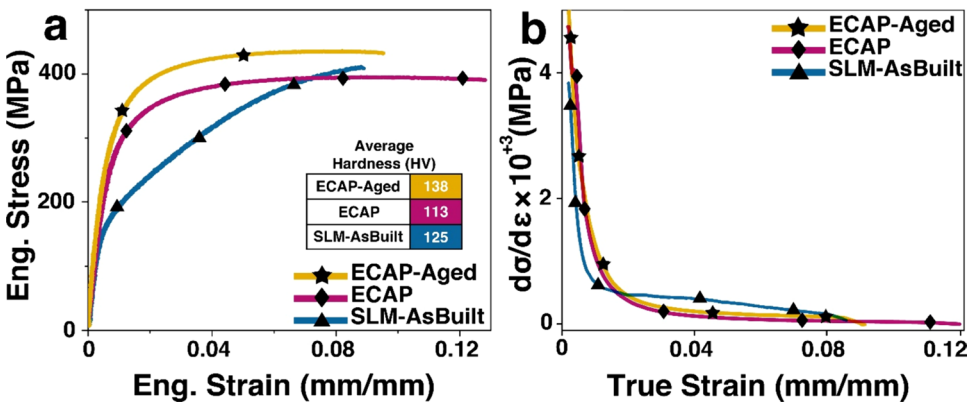

Fig. 3 **a** Engineering stress–strain and **b** strain hardening rate (SHR) curves of the As-built, ECAP, and ECAP-Aged AlSi10Mg samples

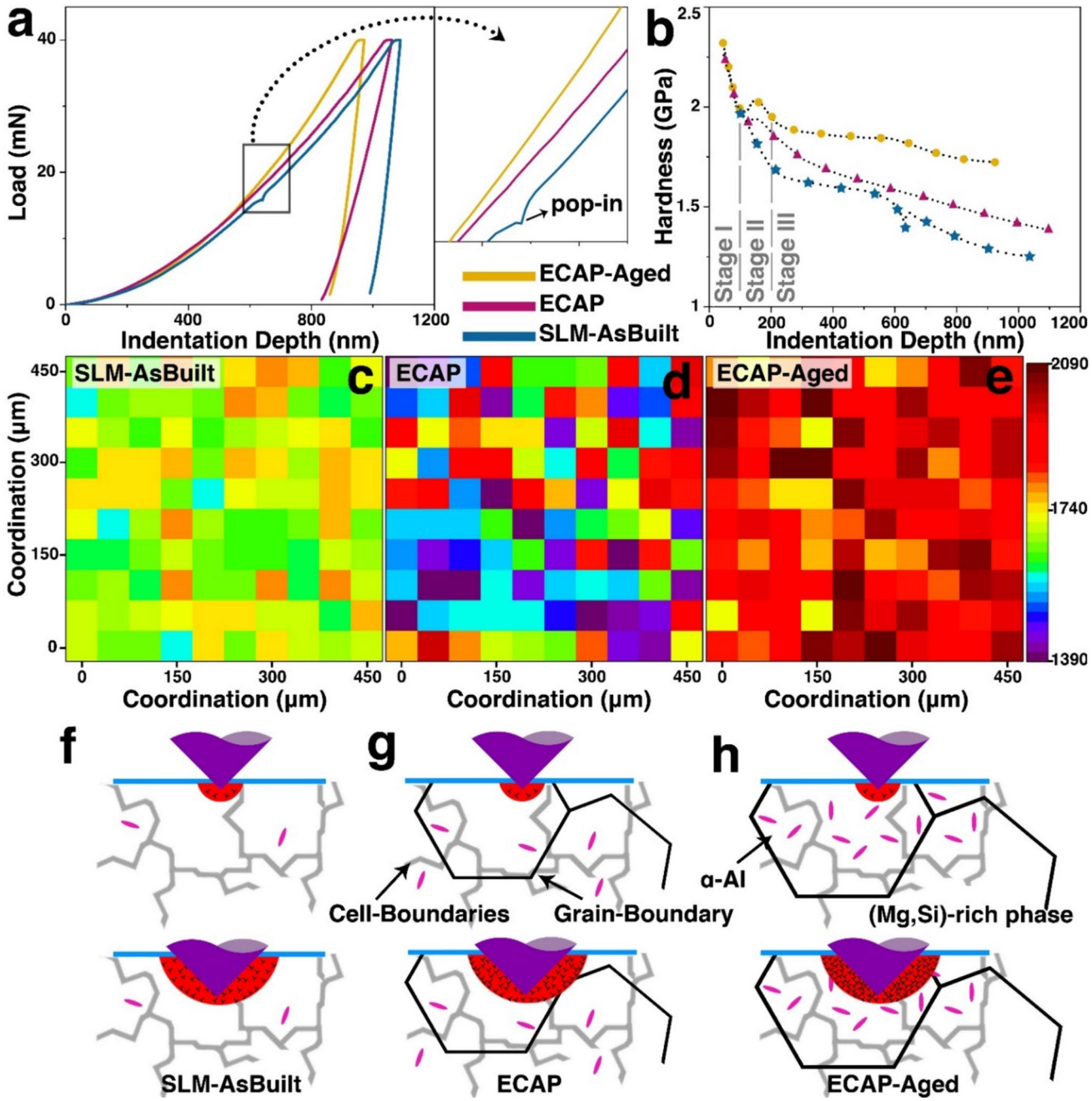

Fig. 4 Nano-indentation test results **a** Load-indentation depth response, **b** hardness-depth response of samples, **c–e** hardness maps, **f–h** schematic representing various microstructure characteristics under loading for the As-built, ECAP, and ECAP-Aged AlSi10Mg samples

intensifies with the application of the aging treatment after SPD. Depicting the nano-indentation maps for all three microstructures shows that the uniformity of the hardness values can be altered by the applied thermo-mechanical processing (see Fig. 4c-e).

Accordingly, results illustrate that the variation in the hardness of the ECAP sample is the highest. This observation can be linked to the higher variation in the KAM value distribution, as represented in Fig. 2c**.** The KAM results illustrate regions with a high density of dislocations besides regions with near-fully-recrystallized structures (Fig. 2c and 2f). In addition, the lack of well-distributed secondary phases can be another factor that leads to this varying nano-mechanical behavior. Therefore, microstructures with higher uniformity in dislocation and (Mg,Si)-rich phase distribution can lead to higher consistency in the nano-indentation response. Comparing the hardness levels for the investigated microstructures shows that the ECAP-Aged sample has the

highest hardness, which is in good agreement with the Vickers hardness results (see Fig. 3a). However, due to the size effect of the nano-indentation, the obtained hardness values are higher than the microhardness results [45].

Figure 4f-h represent the mechanisms involved during deformation by nano-indentation. As shown in Fig. 4b**,** the hardness curves represent multi-stage transitions. This behavior can be rationalized by the variation of the mean free path of dislocations during the progress of the tip of the indenter initiating at the sample's surface. Initially, there are no grain boundaries to limit the dislocation movement in the microstructure (top row in Fig. 4f-h corresponding to Stage 1 in Fig. 4b). However, with a reduction of the grain size to sub-micron levels, dislocations start to pile-up at the grain boundaries. This results in elevated work hardening ability and leads to an increase in the hardness value. With further advancement of the indenter through the microstructure, pile-up stress at the grain boundaries surpasses a critical value, and dislocations start to transit into the neighboring grains. This transition decreases the dislocation density concentrated at the grain boundaries, and the hardness value displayed on the hardness-indentation depth curve starts to decline. Moreover, the existence of secondary phases in the microstructure improves the hardening ability significantly (see Fig. 4g and h). This behavior can be corroborated by comparing the peak heights in ECAP and ECAP-aged samples. In other words, besides the fine grain size, the higher content of (Mg,Si)-rich phase intensifies the peak height observed in the ECAP-Aged samples during the advancement of the indenter in the material, i.e., Stage 2 in Fig. 4b. However, after surpassing a critical value at the pile-up, the dislocations transfer to the next grain causing a reduction in the hardness values (Stage 3 in Fig. 4b).

3.4 Damping Characteristics

The damping behavior of aluminum alloys is closely related to the thermo-elastic damping, viscous damping, dislocation damping (or damping via defects), and grain boundary sliding mechanisms [27]. The dominant mechanisms impacting the damping are considered to be the dislocation density and grain boundary sliding, since the thermo-elastic damping only increases with the increasing frequency under the level of relaxation frequency level [46]. Therefore, it is important to focus on dislocations, grain boundaries and secondary phases in the microstructure, which play significant roles in investigating the damping behavior of the alloy. The internal friction, i.e., Q^{-1}, and storage modulus results of all samples at a 5×10^{-5} strain rate, temperature ranges to 0–300°C, are presented in Fig. 5a-b. The results denoted that elevated temperature also increases the Q^{-1} for all the samples due to the relaxation of the structure contributing to the energy dissipation [47]. In aluminum alloys, this energy dissipation occurs due to the weakened effect of the dislocation damping mechanism and viscous flow at the grain boundaries at elevated temperatures [48]. Throughout the test, when the temperature has reached a maximum of 300°C, the damping capacity of the ECAP sample is about 150% higher than that of the SLM-As-built AlSi10Mg. The severely deformed microstructures of the ECAP and ECAP-aged AlSi10Mg demonstrate improved internal friction exhibiting a decent damping capacity as in the quasi-static mechanical response.

In this respect, ECAP, as a viable processing tool to engineer additive-manufactured microstructures, can be used to enhance the damping capacity. Since ECAP introduces high dislocation density and provides sub-micron grain size refinement, these abundant defects may assist the diffusion process and increase internal friction [49]. The mechanistic effect of dislocations on the damping can be considered at lower temperatures as explained by the Granato-Lücke (G-L) theory [50], such that the solute atoms and vacancies serve as weak pinning points for the dislocation movements and create distortion fields [51]. These points or obstacles impede the movement of the dislocation loops while causing energy dissipation. According to the G-L theory, longer dislocation loops and higher dislocation density improve the damping capacity [27, 52]. Nonetheless, after the temperature is increased, the dislocations start to unpin from the pining points, and the contribution of the dislocations to the damping capacity decreases.

At higher temperatures, the grain boundary sliding mechanism becomes more effective and contributes to the damping capacity [53]. Previous studies have shown that effective grain size reduction via ECAP increases the volume fraction of the grain boundaries, thereby improving the capacity for grain boundary sliding [54]. During severe plastic deformation, highly misoriented grains are established due to intense shear straining. In addition to high dislocation density, this leads to the formation of high-energy grain boundaries with non-equilibrium configurations. In this microstructural state, the application of external stress will cause atomic rearrangements by grain boundary sliding with the movement of atoms in non-equilibrium positions on each other [55]. Accordingly, a prior study has focused on the grain size effect of aluminum with coarse and nano-sized grains compared with their damping properties. The nano-grained aluminum has shown superior damping performance than the coarse-grained sample as attributed to the grain boundary activity [56]. Furthermore, grain size refinement also affects the temperature dependency of the damping behavior. Due to the smaller grain size of the ECAP samples, grain boundary sliding starts at lower temperatures; thus, it enhances the damping capacity of the alloy. However, in the SLM-As-built sample, grain boundary sliding is limited due to its coarser grain size with lower fraction of grain boundaries.

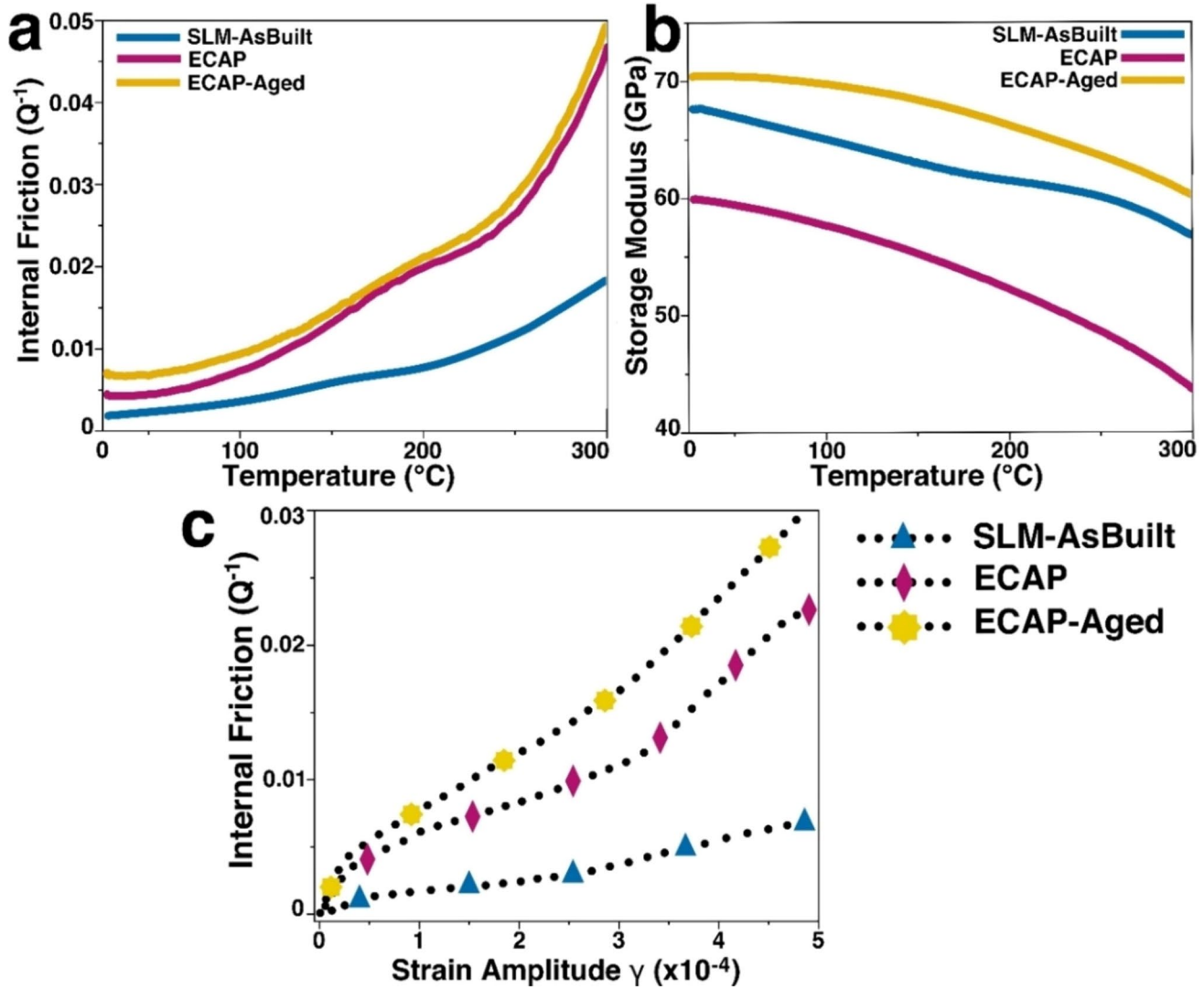

Fig. 5 **a** The internal friction and **b** the storage modulus as a function of temperature for all samples. **c** The internal friction-strain amplitude γ diagram of the samples

The severely deformed microstructure also influences the post-SPD aging characteristics. Secondary phases influence the damping capacity in two avenues. First, they act as obstacles to dislocation movement which lengthens the dislocation loops and provides internal friction, as explained previously. Second, they can hinder grain growth and improve the grain boundary sliding thus, enhance the high-temperature damping capacity of the alloy [57]. It can be seen in Fig. 5a**,** the internal friction of the ECAP-Aged sample is slightly higher than that of the ECAP sample, especially up to 100°C. However, the difference in the storage modulus levels is considerably higher, pointing to the effect of the secondary phase on the ability to store elastic energy to a larger extent. The SLM-As-built sample has higher storage modulus than the ECAP sample as attributed to the higher level of structural relaxation in the severely deformed microstructure of the latter (see Fig. 5b) [11, 58]. Moreover, the storage modulus decreases with increasing temperature as attributed to thermal softening in aluminum alloys [59]. Furthermore, the distribution of the secondary phases is also important for the damping capacity. Coherent particles with uniform distribution are found to be more effective since they act as stronger pinning zones in comparison to that observed for incoherency and/or non-uniform distribution [60]. This behavior is reported in a previous study, in which the coherent particles creating strong pinning points enhance the damping capacity [61]. This is the case in Fig. 2b and 2e, where the relatively more uniform distribution of (Mg,Si)-rich phase in the ECAP-Aged sample is noticeable as compared to that observed in the ECAP sample (see Fig. 2). Thus, it can be concluded that the damping

behavior of the alloy can also be controlled by the distribution of secondary phases to enhance the dislocation pinning effect in the matrix.

Figure 5c shows the variation of the internal friction (Q^{-1}) with the strain amplitude γ at ambient temperature for the As-built, ECAP, and ECAP-Aged samples. The internal friction increases rapidly for the ECAP and ECAP-Aged samples in contrast to the as-built sample. Considering this damping behavior, it can be noted that the ECAP and the ECAP-Aged samples present a strain-dependent behavior, while the SLM-As-built sample demonstrates a slight increase in internal friction at a slower rate. For the ECAP and ECAP-Aged samples, it could be possible that the increased strain level leads to the formation of new dislocation loops, and the damping capacity exhibits a strong strain dependency [37]. In the previous section, the ECAP sample represented a non-uniform hardness distribution, while the ECAP-Aged sample had a uniform distribution, which also indicates microstructural uniformity (see Fig. 4c-e). The slightly higher damping capacity of the ECAP-Aged sample could also be imputed to this uniformly distributed defect substructure [24, 62]. The non-uniform microstructure of the ECAP sample needs relatively higher strain levels, whereas the dislocation substructure of the thermally recovered and uniform microstructure present in the ECAP-Aged sample could be activated at lower strain levels and thus shows a high rate of increase in the damping capacity with the strain level [63].

4 Conclusion

The current work illustrates a systematic approach for studying the effects of severe plastic deformation and post-heat treatment on the additive-manufactured AlSi10Mg alloy with the following conclusions:

i. SPD induced TMP can be utilized to tailor both the monotonic response and the damping characteristics of the additive-manufactured microstructure.
ii. The stress–strain response shows that the yield strength of the as-built condition can be improved up to more than two-folds by the application of four ECAP passes followed by artificial aging.
iii. Improved damping characteristics after aging can be attributed to the differences in the secondary phase distribution and the dislocation density levels of ECAP and ECAP-Aged samples based on their respective KAM values.
iv. The provision of uniform nano-mechanical response reinforces the damping behavior with clear improvement in the internal friction level as shown for the microstructural evolution in the ECAP-Aged sample.

Acknowledgements This work is supported by the BAGEP Award of Bilim Akademisi (The Science Academy), Türkiye. The financial support of Ozyegin University Research Fund is also acknowledged.

Funding Open access funding provided by the Scientific and Technological Research Council of Türkiye (TÜBİTAK).

Declarations

Conflict of interest The authors declare that they have no known competing financial interests or personal relationships that could have appeared to influence the work reported in this manuscript.

Open Access This article is licensed under a Creative Commons Attribution 4.0 International License, which permits use, sharing, adaptation, distribution and reproduction in any medium or format, as long as you give appropriate credit to the original author(s) and the source, provide a link to the Creative Commons licence, and indicate if changes were made. The images or other third party material in this article are included in the article's Creative Commons licence, unless indicated otherwise in a credit line to the material. If material is not included in the article's Creative Commons licence and your intended use is not permitted by statutory regulation or exceeds the permitted use, you will need to obtain permission directly from the copyright holder. To view a copy of this licence, visit http://creativecommons.org/licenses/by/4.0/.

References

1. A. Mishra, R. Agarwal, N. Kumar, A. Rana, A. Kumar Pandey, S.P. Dwivedi, Mater. Today Proc. **47**, 4074 (2021). https://doi.org/10.1016/j.matpr.2021.05.698
2. R. Shanthar, K. Chen, C. Abeykoon, Adv. Eng. Mater. **25**, 2300375 (2023). https://doi.org/10.1002/adem.202300375
3. B. Parvaresh, H. Aliyari, R. Miresmaeili, M. Dehghan, M. Mohammadi, Met. Mater. Int. **29**, 3103 (2023). https://doi.org/10.1007/s12540-023-01444-4
4. D. Zhang, S. Sun, D. Qiu, M.A. Gibson, M.S. Dargusch, M. Brandt, M. Qian, M. Easton, Adv. Eng. Mater. **20**, 1700952 (2018). https://doi.org/10.1002/adem.201700952
5. G.M. Karthik, H.S. Kim, Met. Mater. Int. **27**, 1 (2021). https://doi.org/10.1007/s12540-020-00931-2
6. W.H. Kan, L.N.S. Chiu, C.V.S. Lim, Y. Zhu, Y. Tian, D. Jiang, A. Huang, J. Mater. Sci. **57**, 9818 (2022). https://doi.org/10.1007/s10853-022-06990-7
7. A. Radi, S. Sajadifar, S.V. Seyedmohammadi, M. Krochmal, A. Bolender, T. Wegener, T. Niendorf, G.G. Yapici, Int. J. Fatigue **173**, 107678 (2023). https://doi.org/10.1016/j.ijfatigue.2023.107678
8. A. Radi, P. Asghari-Rad, H.S. Kim, G.G. Yapici, J. Alloys Compd. **905**, 164014 (2022). https://doi.org/10.1016/j.jallcom.2022.164014
9. M. Naseri, M. Reihanian, A.O. Moghaddam, D. Gholami, M. Alvand, E. Borhani, E. Trofimov, Met. Mater. Int. **30**, 412 (2024). https://doi.org/10.1007/s12540-023-01515-6
10. A. Hosseinzadeh, A. Radi, and G. G. Yapici, in *Lect. Notes Mech. Eng.* (2022), pp. 8–12. https://doi.org/10.1007/978-981-16-5763-4_2
11. S.V. Sajadifar, C. Atli, G.G. Yapici, Mater. Lett. **244**, 100 (2019). https://doi.org/10.1016/j.matlet.2019.02.010
12. A. Hosseinzadeh, A. Radi, J. Richter, T. Wegener, S.V. Sajadifar, T. Niendorf, G.G. Yapici, J. Manuf. Process. **68**, 788 (2021). https://doi.org/10.1016/j.jmapro.2021.05.070

13. S.V. Sajadifar, A. Hosseinzadeh, J. Richter, M. Krochmal, T. Wegener, A. Bolender, A. Heidarzadeh, T. Niendorf, G.G. Yapici, Adv. Eng. Mater. **24**, 2200384 (2022). https://doi.org/10.1002/adem.202200384
14. L.F. Wang, J. Sun, X.L. Yu, Y. Shi, X.G. Zhu, L.Y. Cheng, H.H. Liang, B. Yan, L.J. Guo, Mater. Sci. Eng. A **734**, 299 (2018). https://doi.org/10.1016/j.msea.2018.07.103
15. I. Del Castillo, A. Wilson, X. Sun, L. Ader, T. VerKuilen, A. Massar, Y. Li, M. Ebrahim, T. Breman, O.S. Es-Said, J. Mater. Eng. Perform. **32**, 91 (2023). https://doi.org/10.1007/s11665-022-07509-6
16. M.S. Bisht, V. Gaur, I.V. Singh, Mater. Sci. Eng. A **858**, 144157 (2022). https://doi.org/10.1016/j.msea.2022.144157
17. W.J. Hwang, G.B. Bang, S.H. Choa, Met. Mater. Int. **29**, 1311 (2023). https://doi.org/10.1007/s12540-022-01304-7
18. H.M. Joo, W.C. Kim, Y. Jung, H.J. Kim, S.J. Kim, Y.C. Jo, W.H. Yong, D.H. Kim, Met. Mater. Int. **30**, 1294 (2024). https://doi.org/10.1007/s12540-023-01567-8
19. P. Hahner, Acta Mater. **45**, 3695 (1997). https://doi.org/10.1016/s1359-6454(97)00066-9
20. A. Radi, J. Khalil-Allafi, A. Heidarzadeh, G.G. Yapici, M.R. Etminanfar, S.Z. Mozafari, B. Rezaei-Moghadam, Met. Mater. Int. **27**, 3968 (2021). https://doi.org/10.1007/s12540-020-00935-y
21. F. Scalzo, G. Totis, E. Vaglio, M. Sortino, Precis. Eng. **71**, 63 (2021). https://doi.org/10.1016/j.precisioneng.2021.02.010
22. W.P. Syam, W. Jianwei, B. Zhao, I. Maskery, W. Elmadih, R. Leach, Precis. Eng. **52**, 494 (2018). https://doi.org/10.1016/j.precisioneng.2017.09.010
23. D.D.L. Chung, J. Mater. Sci. **36**, 5733 (2001). https://doi.org/10.1023/a:1012999616049
24. C. Isil, A. Radi, S.V. Seyedmohammadi, G.G. Yapici, Mater. Lett. **328**, 133095 (2022). https://doi.org/10.1016/j.matlet.2022.133095
25. F. Rosa, S. Manzoni, R. Casati, Mater. Des. **160**, 1010 (2018). https://doi.org/10.1016/j.matdes.2018.10.035
26. X. Wang, M. Speirs, S. Kustov, B. Vrancken, X. Li, J.P. Kruth, J. Van Humbeeck, Scr. Mater. **146**, 246 (2018). https://doi.org/10.1016/j.scriptamat.2017.11.047
27. C.Y. Xie, R. Schaller, C. Jaquerod, Mater. Sci. Eng. A **252**, 78 (1998). https://doi.org/10.1016/s0921-5093(98)00683-2
28. P.A. Rometsch, Y. Zhu, X. Wu, A. Huang, Mater. Des. **219**, 110779 (2022). https://doi.org/10.1016/j.matdes.2022.110779
29. E.O. Olakanmi, R.F. Cochrane, K.W. Dalgarno, Prog. Mater. Sci. **74**, 401 (2015). https://doi.org/10.1016/j.pmatsci.2015.03.002
30. L. Wang, X. Jiang, Y. Zhu, X. Zhu, J. Sun, B. Yan, Int. J. Adv. Manuf. Technol. **97**, 3535 (2018). https://doi.org/10.1007/s00170-018-2207-3
31. S. Bagherifard, N. Beretta, S. Monti, M. Riccio, M. Bandini, M. Guagliano, Mater. Des. **145**, 28 (2018). https://doi.org/10.1016/j.matdes.2018.02.055
32. M. Cabibbo, R. Montanari, A. Pola, M. Tocci, A. Varone, J. Alloys Compd. **914**, 165361 (2022). https://doi.org/10.1016/j.jallcom.2022.165361
33. C. Colombo, C.A. Biffi, J. Fiocchi, D. Scaccabarozzi, B. Saggin, A. Tuissi, L.M. Vergani, Theor. Appl. Fract. Mech. **107**, 102537 (2020). https://doi.org/10.1016/j.tafmec.2020.102537
34. P. Snopiński, A. Woźniak, M. Pagáč, Materials **14**, 7598 (2021). https://doi.org/10.3390/ma14247598
35. I.Y. Kim, S.C. Park, Y. Kim, D.K. Kim, K.A. Lee, S.J. Oh, B.J. Lee, Alloys Compd. **945**, 169315 (2023). https://doi.org/10.1016/j.jallcom.2023.169315
36. P. Murugesan, V. Satheeshkumar, N. Jeyaprakash, C.H. Yang, S.S. Karuppasamy, Met. Mater. Int. **29**, 2515 (2023). https://doi.org/10.1007/s12540-023-01394-x
37. W.E. Frazier, J. Mater. Eng. Perform. **23**, 1917 (2014). https://doi.org/10.1007/s11665-014-0958-z
38. N.T. Aboulkhair, M. Simonelli, L. Parry, I. Ashcroft, C. Tuck, R. Hague, Prog. Mater. Sci. **106**, 100578 (2019). https://doi.org/10.1016/j.pmatsci.2019.100578
39. Z. Jiang, Y. Li, H. Luo, B. Zhou, Y. Liang, Y. Liang, Met. Mater. Int. **28**, 2934 (2022). https://doi.org/10.1007/s12540-022-01199-4
40. L. Thijs, K. Kempen, J.P. Kruth, J. Van Humbeeck, Acta Mater. **61**, 1809 (2013). https://doi.org/10.1016/j.actamat.2012.11.052
41. G.G. Yapici, I.J. Beyerlein, I. Karaman, C.N. Tomé, Acta Mater. **55**, 4603 (2007). https://doi.org/10.1016/j.actamat.2007.03.031
42. G.S. Dyakonov, S. Mironov, I.P. Semenova, R.Z. Valiev, S.L. Semiatin, Acta Mater. **173**, 174 (2019). https://doi.org/10.1016/j.actamat.2019.05.014
43. I. Mazurina, T. Sakai, H. Miura, O. Sitdikov, R. Kaibyshev, Mater. Trans. **50**, 101 (2009). https://doi.org/10.2320/matertrans.md200807
44. K. Zyguła, B. Nosek, H. Pasiowiec, N. Szysiak, World Sci. News **104**, 466 (2018)
45. R. Rodríguez, I. Gutierrez, Mater. Sci. Eng. A **361**, 377 (2003). https://doi.org/10.1016/s0921-5093(03)00563-x
46. G.C. Li, Y. Ma, X.L. He, W. Li, P.Y. Li, Trans. Nonferrous Met. Soc. China **22**, 1112 (2012). https://doi.org/10.1016/s1003-6326(11)61291-0
47. S.G. Ma, P.K. Liaw, M.C. Gao, J.W. Qiao, Z.H. Wang, Y. Zhang, J. Alloys Compd. **604**, 331 (2014). https://doi.org/10.1016/j.jallcom.2014.03.050
48. Z. Li, H. Yan, J. Chen, W. Xia, H. Zhu, B. Su, X. Li, J. Alloys Compd. **908**, 164677 (2022). https://doi.org/10.1016/j.jallcom.2022.164677
49. S.H. Chang, S.K. Wu, W.L. Tsai, J.Y. Wang, J. Alloys Compd. **487**, 142 (2009). https://doi.org/10.1016/j.jallcom.2009.08.006
50. A. Granato, K. Lücke, J. Appl. Phys. **27**, 583 (1956). https://doi.org/10.1063/1.1722436
51. X. Li, Y. Fan, X. Zhao, R. Ma, A. Du, X. Cao, H. Ban, Metals (Basel). **9**, 1195 (2019). https://doi.org/10.3390/met9111195
52. Z. Li, H. Yan, J. Chen, W. Xia, B. Su, L. Zhao, M. Song, Met. Mater. Int. **27**, 3155 (2021). https://doi.org/10.1007/s12540-020-00695-9
53. B.H. Luo, Z.H. Bai, Y.Q. Xie, Mater. Sci. Eng. A **370**, 172 (2004). https://doi.org/10.1016/j.msea.2002.12.007
54. M. Kawasaki, T.G. Langdon, J. Mater. Sci. **48**, 4730 (2013). https://doi.org/10.1007/s10853-012-7104-9
55. Y. Koizumi, M. Ueyama, N. Tsuji, Y. Minamino, J. Alloys Compd. **355**, 47 (2003). https://doi.org/10.1016/s0925-8388(03)00265-2
56. H. Jang, K. Choi, J. Shin, D. Bae, H. Choi, Arch. Metall. Mater. **64**, 475 (2019). https://doi.org/10.24425/amm.2019.127562
57. H.J. Jiang, C.Y. Liu, B. Zhang, P. Xue, Z.Y. Ma, K. Luo, M.Z. Ma, R.P. Liu, Mater. Charact. **131**, 425 (2017). https://doi.org/10.1016/j.matchar.2017.07.037
58. D.R. Ni, J.J. Wang, Z.Y. Ma, J. Mater. Sci. Technol. **32**, 162 (2016). https://doi.org/10.1016/j.jmst.2015.12.013
59. Y. Cao, X. Lin, Q.Z. Wang, S.Q. Shi, L. Ma, N. Kang, W.D. Huang, J. Mater. Sci. Technol. **62**, 162 (2021). https://doi.org/10.1016/j.jmst.2020.04.066
60. C. Do Lee, Mater. Sci. Eng. A **394**, 112 (2005). https://doi.org/10.1016/j.msea.2004.11.033
61. P.Y. Li, H.J. Yu, S.C. Chai, Y.R. Li, Scr. Mater. **49**, 819 (2003). https://doi.org/10.1016/s1359-6462(03)00483-4
62. H. Wang, W. Zhang, P. Gao, Q. Xiang, Y. Qu, J. Cheng, Y. Ren, B. Yu, K. Qiu, J. Alloys Compd. **876**, 159991 (2021). https://doi.org/10.1016/j.jallcom.2021.159991
63. C. Azcotia, A. Karimi, J. Alloys Compd. **310**, 160 (2000). https://doi.org/10.1016/s0925-8388(00)00938-5

Publisher's Note Springer Nature remains neutral with regard to jurisdictional claims in published maps and institutional affiliations.